Journal of
*Marine Science and Engineering*

MDPI

*Article*

# Numerical Simulations on the Flooding into a Damaged Cabin with a Flexible Bulkhead Based on the Mixed-Mode Function-Modified MPS Method

**Jinxin Wu [1], Guiyong Zhang [1,2,*], Yichen Jiang [1] and Xi Yang [1]**

[1] State Key Laboratory of Structural Analysis for Industrial Equipment, School of Naval Architecture Engineering, Dalian University of Technology, Dalian 116024, China
[2] Collaborative Innovation Center for Advanced Ship and Deep-Sea Exploration, Shanghai 200240, China
* Correspondence: gyzhang@dlut.edu.cn

**Abstract:** Floodwater entering the damaged cabin and impacting the bulkhead can cause damage to the watertight compartment and affect the survival of the ship. The elastic deformation of the bulkhead can slow down the impact and affect the flow field, which affects the hydrodynamic distribution inside the cabin. In this work, numerical simulations on the flooding phenomena into the damaged cabin with various stiffness, watertight bulkheads are carried out by using the mixed-mode function-modified moving particle semi-implicit (MPS) method, with the objective of investigating the influence of the stiffness of the watertight bulkheads on the structural impact load. Firstly, the numerical model based on the MPS method is set up to predict the dam-break wave impact load on an elastic plate and compared with the experimental measurements to verify the feasibility of the method. Then, the evolution of the flooding process of the damaged cabin with four different stiffnesses are simulated and the impact pressure on the bulkhead is predicted and compared. It is found that the flexible watertight bulkheads not only can reduce the peak pressure acting on it, but also have an effect on the hydrodynamic pressure distribution of the entire cabin. This implies that properly selected stiffness and material properties of watertight bulkheads can mitigate the impact of flooding on the damaged cabin's bulkheads.

**Keywords:** moving particle semi-implicit (MPS) method; damaged cabin; flooding; flexible bulkhead; fluid–structure interaction

check for updates

**Citation:** Wu, J.; Zhang, G.; Jiang, Y.; Yang, X. Numerical Simulations on the Flooding into a Damaged Cabin with a Flexible Bulkhead Based on the Mixed-Mode Function-Modified MPS Method. *J. Mar. Sci. Eng.* **2022**, *10*, 1582. https://doi.org/10.3390/jmse10111582

Academic Editor: Alfredo L. Aretxabaleta

Received: 20 September 2022
Accepted: 20 October 2022
Published: 26 October 2022

**Publisher's Note:** MDPI stays neutral with regard to jurisdictional claims in published maps and institutional affiliations.

**Copyright:** © 2022 by the authors. Licensee MDPI, Basel, Switzerland. This article is an open access article distributed under the terms and conditions of the Creative Commons Attribution (CC BY) license (https://creativecommons.org/licenses/by/4.0/).

## 1. Introduction

Accidents such as collisions and grounding occur on a regular basis when ships are at sea. Some of these will cause ship damage and a large amount of seawater to flood into the cabin in a short period of time, potentially causing the ship to become unstable or capsize. Subdivision design is used by the majority of modern large-scale ships to improve the survivability of damaged ships. In the event of hull damage, watertight bulkheads are critical to ship survival [1]. However, once the cabin is damaged, high-speed flooding can lead to a large impact load on the subdivision baffle and other parts of the bulkhead, resulting in the structural response of the entire ship, or even hull structure destruction. Therefore, it is essential to research the effects of flooding, forecast the magnitude of the impact load, and finally mitigate it.

The majority of existing studies on the phenomenon of flooding into the damaged cabin, however, focus on the ship's behavior and movement [2–5], whereas hydrodynamic research primarily focuses on tank sloshing in regular motion, such as the translation or shaking of sine or cosine law [6–10]. The complexity of the transient motion characteristics of the flooding in the cabin, on the other hand, makes it difficult to reduce to a simple mathematical model. As a result, some researchers conducted additional in-depth studies. Huang et al. [11] studied the dynamic characteristics of this water spike during the early flooding process by a three-dimensional fast multipole boundary element method (FMBEM), based on the potential theory, and revealed that the water flooding spike has complex and non-linear dynamic behavior. Bennett and Phillips [12] conducted an experimental investigation on the influence of floodwater and transient flooding on the motions and structural response of a ship hull following a grounding incident. Results show that floodwater can have a significant effect on the magnitude of ship responses. Rodrigues and Soares [13] studied the progression of transient still-water vertical loads throughout the flooding process for a damaged shuttle tanker in full-load condition, determined and analyzed the probability and magnitude of higher intermediate loads and the main effects of the damage parameters and the factor interactions. Yu et al. [14] used the commercial software STAR-CCM+ to simulate the time domain of the instantaneous asymmetrical water inflow process of a 28.8 m breeding care boat in the Bohai Sea under transverse wave conditions, and obtained the variation of the boat's pressure distribution during the cabin flooding process. Cao et al. [15] developed an SPH model to study the dynamic response of the damaged ship in beam seas. It is revealed that the liquid loading conditions on the dynamic response of the damaged ship in regular beam waves. Gu et al. conducted an experimental study [16] and showed that the ingress and egress of floodwater and its interaction with the ship's motions significantly affect the impact loads acting on the ship. Siddiqui et al. [17] performed a series of forced oscillatory heave tests in a wave flume on a thin-walled prismatic hull form. The presented results demonstrate the occurrence of sloshing and piston-mode resonances in the tests and their influence on the hydrodynamic loads of a damaged ship.

Despite this fact, experimental methods have limitations, such as the high cost and complexity of experiment preparation, etc. The application of conventional computational fluid dynamics (CFD) methods is still constrained by the variability of flow morphology and the complexity of interface tracking, despite the researchers' presentation of a number of interface-capturing technologies [18–22]. As the well-known meshless methods, MPS [23,24] and smoothed particle hydrodynamics (SPH) [25–27] do not employ the computational grid and are not required to deal with the nonlinear convective term in the momentum equation, making it better to handle the moving interface with very large deformations and large fluid motion. As a result, it is very applicable to the issue examined in this paper, which is the interaction between flexible bulkheads and flood. The particle methods have been successfully applied to a wide range of highly non-linear fluid–structure interaction problems, such as sloshing in partially filled tanks [6,7], the slamming phenomenon during the water entry process [28–30], and interactions between an elastic gate with a released water column [30–33], etc. In contrast to SPH, which solves the equation of state (EoS), the MPS method employs the pressure Poisson equation (PPE) for pressure computation, allowing for a larger time step. The implicit solution of PPE, on the other hand, can obtain more accurate pressure. The accuracy and stability of the MPS method have been greatly improved in recent years, with the efforts of many scholars [34–45]. We have previously used in-house code to investigate problems involving fluid–solid interaction, such as slamming during water entry [28], and obtained convincing results.

In this paper, we investigate the effects of an elastic watertight bulkhead on pressure distribution in the transient stage [3] of the flooding process for a damaged ship cabin using a numerical solver that coupled the modified MPS method and the modal superposition (rigid and flexible) method. It should be noted that the material models used in this paper are ideal, and the structures will not fail within the numerical simulation's deformation range. The rest of the paper is organized as follows: Section 2 introduces the fluid and structure numerical models; the validation of the numerical models and the detailed discussion of the simulation results are provided in Section 3; and the last section documents the main conclusions.

## 2. Numerical Model

In the present study, a numerical solver, which coupled the modified MPS method and the modal superposition method [46], is used to numerically simulate the water entering of the damaged cabin with a flexible watertight bulkhead. We will give a brief description of the numerical method in this section.

### 2.1. Present MPS Method

According to our previous study [5], the viscosity effect during the water entry of a damaged cabin is negligible; therefore, the incompressible continuity equation and the inviscid Navier–Stokes equation in the Lagrangian framework are used in this study, and are expressed as follows:

$$\begin{array}{c} \nabla \cdot \boldsymbol{u} = 0 \ (1a) \\ \frac{D\boldsymbol{u}}{Dt} = -\frac{1}{\rho}\nabla P + \boldsymbol{g} \ (1b) \end{array} \tag{1}$$

where $\boldsymbol{u}$, $\rho$, $P$, $\boldsymbol{g}$, and $\frac{D}{Dt}$ represent the velocity vector, the density of the fluid, the pressure, the gravitational acceleration (9.81 m/s$^2$), and the material derivative, respectively.

The computational domain is discretized by a number of particles. The particles interact with one another during the calculation process according to a weight function (or kernel function).

$$W(r_{ij}) = \begin{cases} \frac{r_e}{r_{ij}} - 1 & 0 \le r_{ij} \le r_e \\ 0 & r_{ij} \ge r_e \end{cases} \tag{2}$$

where $r_{ij} = |\boldsymbol{r}_j - \boldsymbol{r}_i|$ is the spacing between particles $i$ and $j$, and $\boldsymbol{r}$ is the position vector of the corresponding particle. $r_e$ is the effective radius, usually set to 2.1 $l_0$ ~ 4.0 $l_0$.

In the MPS method, continuous fluid can be represented by physical quantities of mass, coordinates, velocity, and pressure for particles. All of the terms in governing equations are described as the interaction of neighboring particles. The gradient term, Laplacian term, and divergence term of the *i-th* particle is modeled as follows:

$$\begin{array}{c} \langle \nabla \phi \rangle_i = \frac{d}{n^0} \sum\limits_{j \ne i} \nabla \phi_{ij} \frac{(\boldsymbol{r}_j - \boldsymbol{r}_i)}{|\boldsymbol{r}_j - \boldsymbol{r}_i|} W(|\boldsymbol{r}_j - \boldsymbol{r}_i|) \ \ (3a) \\ \langle \nabla^2 \phi \rangle_i = \frac{2d}{n^0 \lambda} \sum\limits_{j \ne i} (\phi_j - \phi_i) W(|\boldsymbol{r}_j - \boldsymbol{r}_i|) \ \ (3b) \\ \langle \nabla \cdot \boldsymbol{u} \rangle_i = \frac{d}{n^0} \sum\limits_{j \ne i} \frac{(\boldsymbol{r}_j - \boldsymbol{r}_i) \cdot (\boldsymbol{u}_j - \boldsymbol{u}_i)}{|\boldsymbol{r}_j - \boldsymbol{r}_i|^2} W(|\boldsymbol{r}_j - \boldsymbol{r}_i|) \ \ (3c) \end{array} \tag{3}$$

where $\phi$ symbolizes the arbitrary scalar variable of the particles; $d$ and $n^0$ equal the number of space dimensions and the initial particle number density for incompressible flow, respectively; $\hat{P}_i$ is defined as $\hat{P}_i = \min(P_j)$ [23,24]. The particle density $n$ and parameter $\lambda$ are defined below:

$$\begin{array}{c} \langle n \rangle_i = \sum\limits_{j \ne i} W(r_{ij}) \ \ (4a) \\ \lambda = \frac{\sum\limits_{j \ne i} W(r_{ij}) {r_{ij}}^2}{\sum\limits_{j \ne i} W(r_{ij})} \ \ (4b) \end{array} \tag{4}$$

The calculation process of the MPS method is mainly divided into two steps. Firstly, the viscous force (if considered) and gravity are calculated, and the velocity and position of the particles are updated on this basis, and the updated particles are called intermediate state particles; secondly, the pressure $P$ is obtained by solving the pressure Poisson equation by enforcing the incompressibility conditions in the intermediate state, and the particle position and other relevant physical quantities are updated again. In this study, to control the nonphysical oscillation of the particle pressure, the following pressure Poisson equation [47] was applied:

$$\nabla^2 P^{k+1} = (1-\alpha)\rho \frac{\nabla \cdot \boldsymbol{u}^*}{\Delta t} + \alpha\rho \frac{n^0 - n^k}{n^0 \Delta t^2} \tag{5}$$

where $\boldsymbol{u}^*$ is the intermediate velocity of a particular time step, $\Delta t$ is the size of a single time step, superscripts $k$ and $k+1$ are, respectively, the $k^{th}$ and $(k+1)^{th}$ time steps, and $\alpha$ is a coefficient normally far smaller than 1.

Furthermore, some other technologies are used in the MPS model of this study, including particle shifting, adjacent particle searching, Neumann-type boundary conditions, etc., which makes the simulation of the flow field with violent free-surface motion more accurate and stable compared with the original MPS [23,24]. In view of the length problem, we will not repeat them here, and more details are given in Ref. [47].

### 2.2. Coupled Rigid-Body/Elastic Modes Method

Since the flexibility of the watertight bulkhead structure is considered in this study, the coupled rigid-body/elastic modes model presented by Sun [46] is applied. We will give a brief derivation below.

Two types of coordinate systems are used for the description of the damaged cabin structure, which includes a global system, X−O−Y, and a local system, $s - o_F - w$, as shown in Figure 1. The rigid/flexible watertight bulkhead is represented by the fixed–fixed-type beam model. The dynamics of the damaged cabin could be represented by the deflection of the beam $\eta$ and the position of the gravity center $o_R$.

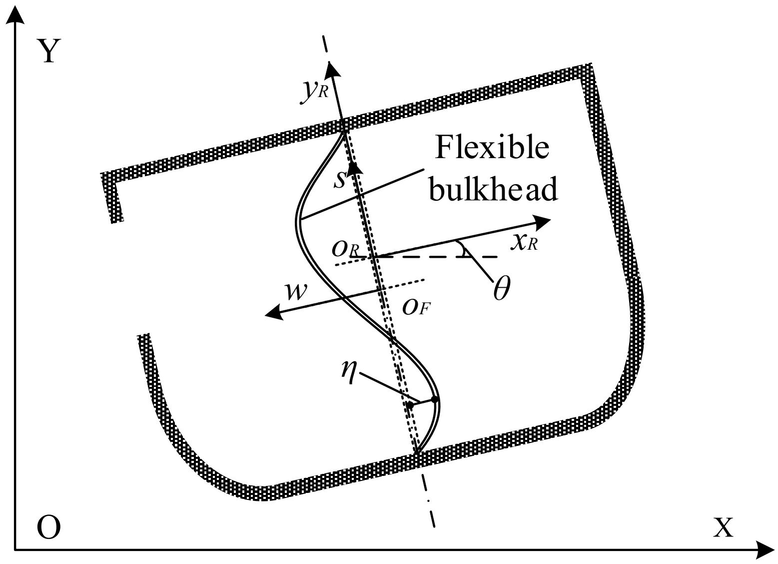


**Figure 1.** Sketch of the model for the damaged cabin with a rigid/flexible bulkhead.

For a flexible bulkhead structure, its motion could be described by the coordinates of the points on the central line, $\boldsymbol{X}_F = [X_F(t), Y_F(t)]^T$, as:

$$\boldsymbol{X}_F = \boldsymbol{X}_R + \mathbf{R}\boldsymbol{o}_{R-F} + \mathbf{R}\boldsymbol{\xi} \tag{6}$$

where $\boldsymbol{X}_R = [X_R,\ Y_R]$ is the coordinate of the local system origin $o_R$ in the global system. $\boldsymbol{o}_{R-F} = \left[x_{of},\ y_{of}\right]$ is the vector from $\boldsymbol{o}_R$ to $\boldsymbol{o}_F$. $\mathbf{R}$ is the rotation matrix that relates the local system $s - o_F - w$ to the local system $x_R - o_R - y_R$ and global system X−O−Y, in this study, is defines as:

$$\mathbf{R} = \begin{bmatrix} 0 & -1 \\ 1 & 0 \end{bmatrix} \tag{7}$$

$\boldsymbol{\xi}$ is the coordinate of the points on the beam's central line in the local system:

$$\boldsymbol{\xi} = [s, \eta]^T \tag{8}$$

The elastic deformation $\eta$ is represented by the modal superposition approach. To be more specific, the spatial and time dimensions of $\eta$ are treated separately by a set of mode function $\boldsymbol{\Phi} = [\phi_1(s),\ \phi_2(s),\ \phi_3(s),\ \ldots,\ \phi_N(s)]^T$ and the corresponding general coordinates $\mathbf{q} = [q_1(t),\ q_2(t),\ q_3(t),\ \ldots,\ q_N(t)]^T$. $N$ is the number of modes that has been taken into account. Therefore, the deflection along the beam is formulated as below:

$$\eta(s,t) = \boldsymbol{\Phi}^T \mathbf{q} \tag{9}$$

According to the extended Hamilton's principle [48], the motion of the whole cabin system could be described by the Lagrange's equation, as provided in Equation (10):

$$\frac{d}{dt}\left(\frac{\partial T}{\partial \dot{\mathbf{X}}}\right) + \frac{\partial V}{\partial \mathbf{X}} - \frac{\partial T}{\partial \mathbf{X}} = \mathbf{Q} \tag{10}$$

Where $T$ and $V$ represent the kinetic and potential energy of the whole structure system, respectively. If only the first three-order flexible modes, i.e., $q_1$, $q_2$, and $q_3$, are used, $\mathbf{X} = [X,\ Y,\ \theta,\ q_1,\ q_2,\ q_3]$ denotes the general coordinates, where $X$ and $Y$ are coordinates of the origin $o_R$ in the global system X−O−Y, respectively. $\theta$ denotes the rotational angle from the X-axis in the global system to the $x_R$-axis in the local system. $\mathbf{Q} = [Q_1,\ Q_2,\ Q_3,\ Q_4,\ Q_5,\ Q_6]$ indicates the non-conservative forces corresponding to each coordinate mentioned above.

The mode shape functions need to satisfy the following orthogonal conditions in Equations (11) and (12):

$$\int_f \boldsymbol{\Phi}\boldsymbol{\Phi}^T \rho_l ds = \mathbf{I}_N \tag{11}$$

$$\int \left(\frac{d^2\boldsymbol{\Phi}}{ds^2}\right) EJ \left(\frac{d^2\boldsymbol{\Phi}}{ds^2}\right)^T ds = \boldsymbol{\Lambda},\quad \boldsymbol{\Lambda} = diag\left(\omega_k^2\right),\quad k = 1,2,3\ldots N \tag{12}$$

where $\rho_l$, $E$, and $J$ are the line density, Young's modulus, and the second moment of the beam's cross section, respectively; $\omega_k$ stands for the $k^{th}$ natural circular frequency of the beam and $\mathbf{I}_N$ is the $N \times N$ identity matrix. The fixed–fixed-type beam is used to represent the bulkhead structure, and the mode shape function is provided in Equation (13):

$$\begin{aligned} \phi_i &= \tfrac{1}{\sqrt{M_f}}[\cosh(\kappa_i x) - \cos(\kappa_i x) - \sigma_i(\sinh(\kappa_i x) - \sin(\kappa_i x))] \\ \sigma_i &= \tfrac{\cos(\kappa_i l) - \cosh(\kappa_i l)}{\sin(\kappa_i l) - \sinh(\kappa_i l)} \end{aligned} \tag{13}$$

where $l$ is the length of the beam model (i.e., the height of the bulkhead in 2D models) and $x$ is the distance from the origin of $s - o_F - w$ system to any point on the model. The parameter $\kappa_i l$ corresponding to the first three flexible natural frequency are as follows:

$$\begin{aligned} \kappa_1 l &= 4.7300407446 \\ \kappa_2 l &= 7.8532046242 \\ \kappa_3 l &= 10.9956078382 \end{aligned} \tag{14}$$

Moreover, in order to simplify the governing equations below, we will introduce the following definitions:

$$\begin{aligned} \boldsymbol{\psi}_0 &= [\psi_{01},\ \psi_{02},\ \psi_{03},\ \cdots,\ \psi_{0N}] = \int \boldsymbol{\Phi}\rho_l ds \\ \boldsymbol{\psi}_1 &= [\psi_{11},\ \psi_{12},\ \psi_{13},\ \cdots,\ \psi_{1N}] = \int s\boldsymbol{\Phi}\rho_l ds \end{aligned} \tag{15}$$

In the present study, as no concentrated force or moment is applied on the whole structure, if the mode function is chosen up to three order, the governing motion equations for the cabin are obtained:

$$\begin{aligned} & M_F\ddot{X}_R - M_F\dot{\theta}^2\left(x_{of}\cos\theta - y_{of}\sin\theta\right) - M_F\ddot{\theta}\left(x_{of}\sin\theta + y_{of}\cos\theta\right) \\ & +\left(\dot{\theta}^2\cos\theta + \ddot{\theta}\sin\theta\right)(\psi_{01}q_1 + \psi_{02}q_2 + \psi_{03}q_3) \\ & +2\dot{\theta}\sin\theta(\psi_{01}\dot{q}_1 + \psi_{02}\dot{q}_2 + \psi_{03}\dot{q}_3) \\ & -\cos\theta(\psi_{01}\ddot{q}_1 + \psi_{02}\ddot{q}_2 + \psi_{03}\ddot{q}_3) + M_R\ddot{X}_R = Q_1 \end{aligned} \tag{16}$$

$$\begin{aligned} & M_F\ddot{Y}_R - M_F\dot{\theta}^2\left(x_{of}\sin\theta + y_{of}\cos\theta\right) + M_F\ddot{\theta}\left(x_{of}\cos\theta - y_{of}\sin\theta\right) \\ & +\dot{\theta}^2\sin\theta(\psi_{01}q_1 + \psi_{02}q_2 + \psi_{03}q_3) - \ddot{\theta}\cos\theta(\psi_{01}q_1 + \psi_{02}q_2 + \psi_{03}q_3) \\ & -2\dot{\theta}\cos\theta(\psi_{01}\dot{q}_1 + \psi_{02}\dot{q}_2 + \psi_{03}\dot{q}_3) - \sin\theta(\psi_{01}\ddot{q}_1 + \psi_{02}\ddot{q}_2 + \psi_{03}\ddot{q}_3) \\ & +M_R\ddot{Y}_R + \left(M_R + M_f\right)g = Q_2 \end{aligned} \tag{17}$$

$$\begin{aligned} & M_F\left[x_{of}\left(-\ddot{X}_R\sin\theta + \ddot{Y}_R\cos\theta\right) - y_{of}\left(\ddot{X}_R\cos\theta + \ddot{Y}_R\sin\theta\right)\right] \\ & +M_F\ddot{\theta}\left(x_{of}^2 + y_{of}^2\right) - 2\dot{\theta}x_{of}(\psi_{01}\dot{q}_1 + \psi_{02}\dot{q}_2 + \psi_{03}\dot{q}_3) \\ & +y_{of}(\psi_{01}\ddot{q}_1 + \psi_{02}\ddot{q}_2 + \psi_{03}\ddot{q}_3) + \ddot{\theta}I_R + M_F\left(x_{of}\cos\theta + y_{of}\sin\theta\right) \\ & +\left(\ddot{X}_R\sin\theta - \ddot{Y}_R\cos\theta\right)(\psi_{01}q_1 + \psi_{02}q_2 + \psi_{03}q_3) \\ & -2\ddot{\theta}x_{of}(\psi_{01}q_1 + \psi_{02}q_2 + \psi_{03}q_3) + \ddot{\theta}I_f + \ddot{\theta}(q_1^2 + q_2^2 + q_3^2) \\ & +2\dot{\theta}(\dot{q}_1q_1 + \dot{q}_2q_2 + \dot{q}_3q_3) + (\psi_{11}\ddot{q}_1 + \psi_{12}\ddot{q}_2 + \psi_{13}\ddot{q}_3) = Q_3 \end{aligned} \tag{18}$$

$$\begin{aligned} & -\left(\ddot{X}_R\cos\theta + \ddot{Y}_R\sin\theta\right)\psi_{01} + \ddot{\theta}y_{of}\psi_{01} + \dot{\theta}^2x_{of}\psi_{01} + \ddot{\theta}\psi_{11} \\ & -\dot{\theta}^2q_1 + \ddot{q}_1 + \omega_1^2q_1 = Q_4 \end{aligned} \tag{19}$$

$$\begin{aligned} & -\left(\ddot{X}_R\cos\theta + \ddot{Y}_R\sin\theta\right)\psi_{02} + \ddot{\theta}y_{of}\psi_{02} + \dot{\theta}^2x_{of}\psi_{02} + \ddot{\theta}\psi_{12} \\ & -\dot{\theta}^2q_2 + \ddot{q}_2 + \omega_2^2q_2 = Q_5 \end{aligned} \tag{20}$$

$$
\begin{aligned}
&-\left(\ddot{X}_R\cos\theta+\ddot{Y}_R\sin\theta\right)\psi_{03}+\ddot{\theta}y_{of}\psi_{03}+\dot{\theta}^2x_{of}\psi_{03}+\ddot{\theta}\psi_{13} \\
&-\dot{\theta}^2q_3+\ddot{q}_3+\omega_3^2q_3=Q_6
\end{aligned} \tag{21}
$$

where $M_F$ and $M_R$ are the masses for flexible and rigid parts, respectively.

The detailed derivation is provided in Appendix A. The governing equations, Equations (16)–(21), are solved at each FSI iterations using the Newmark method [49] and Newton–Raphson methods. For the fluid–structure interaction process, more detailed information can be found in Ref. [46].

## 3. Results and Discussion

### 3.1. Validation of the Present Numerical Model

To verify our numerical model, a numerical simulation of a dam-break wave impact on an elastic plate [50] is performed and the results are compared with their corresponding experimental data. As shown in Figure 2, the computational domain is 0.584 × 0.356 m, and the initial water column has the dimensions 0.146 × 0.292 m. The elastic plate is placed on the bottom at a distance of 0.286 m to the left wall of the tank. The width and the height of the plate are 0.012 and 0.08 m, respectively. The density and Young's modulus of the elastic plate are 2500 $kg/m^3$ and $10^6$ $N/m^2$, respectively. Three particle spacings, i.e., 0.004 m, 0.002 m, and 0.001 m, are selected to test the convergence of the numerical results.

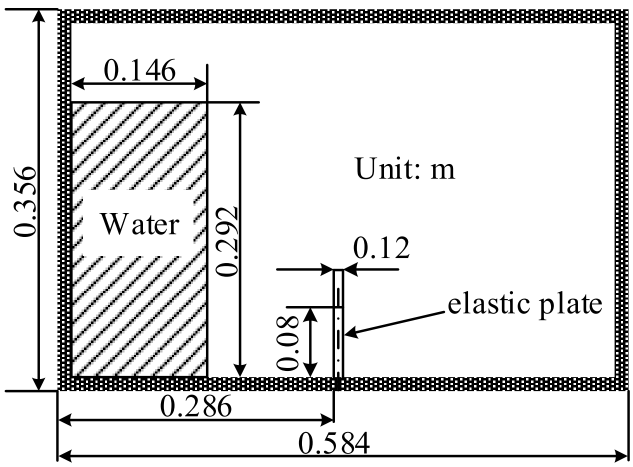


**Figure 2.** Simulation model of the water column with an elastic plate.

The water column on the left will collapse and impact the elastic plate fixed at the bottom during the simulation, resulting in the deformation of the solid structure and fragmentation of the water body. Figure 3 shows the comparison of the water profile between numerical and experimental results [51]. The shapes of the water surface predicted by the present model agree well with video images of the experiment during the process.

Figure 4 shows the displacement of the upper left corner of the elastic plate versus time. The particle spacings, 0.001 m and 0.002 m, are very close and show good agreement with the ANSYS results and FE-SPH, which indicates good convergence and good accuracy of the MPS method. The results of this paper are slightly different from those of other methods during $t$ = 0.3–0.4 s, which could be attributed to the simplification of bending by the Euler–Bernoulli beam model.

As the pressure simulation of the method had been verified many times in our previous study [28,53], it will not be repeated herein. Sections 3.2 and 3.3 have shown that the present method is effective and independent of particle spacing. Therefore, we will adopt this model to study the problem of damaged cabin water entry in the following sub-sections.

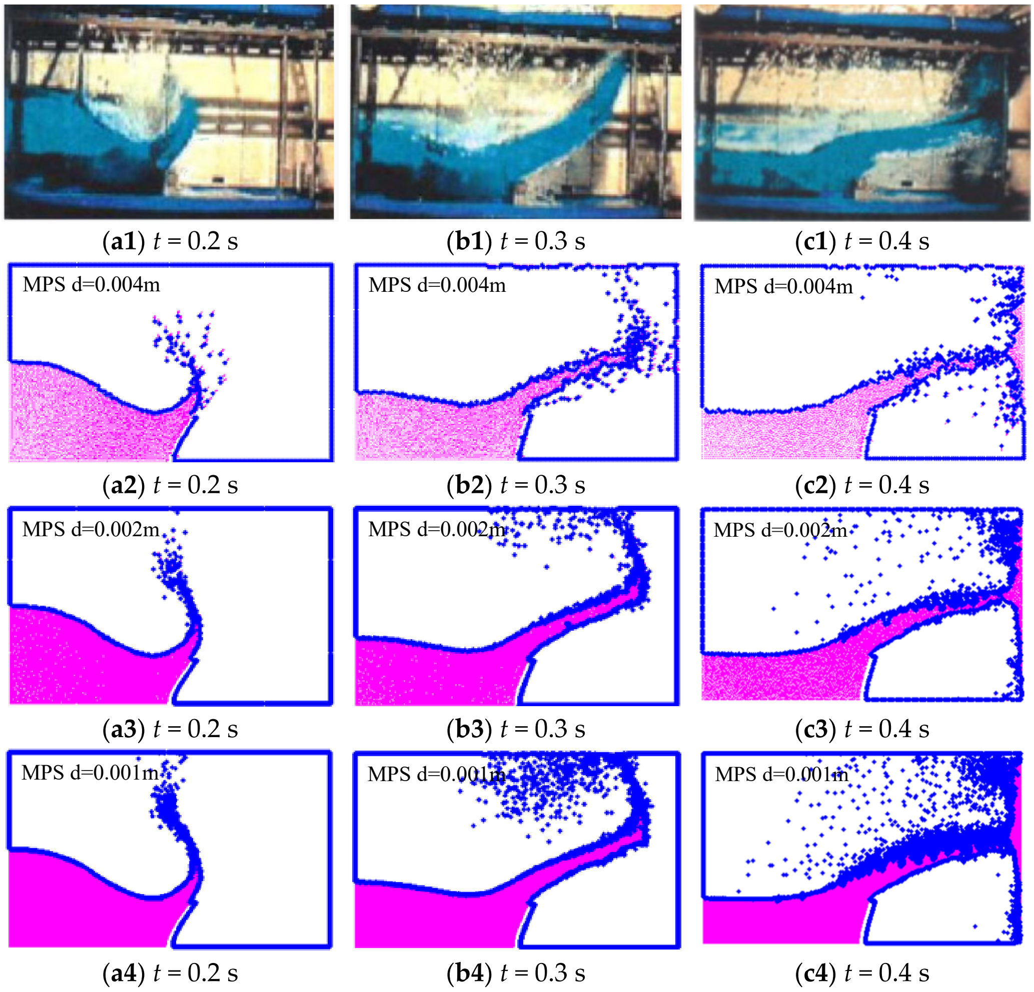


**Figure 3.** Results comparison of water profile of experiment with simulations, where (**a1**,**b1**,**c1**) are the experiment results, (**a2**–**a4**,**b2**–**b4**,**c2**–**c4**) are the MPS results.

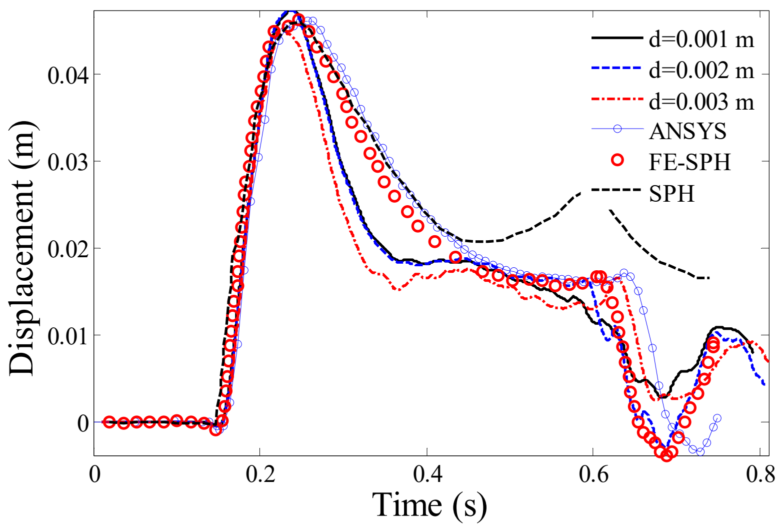


**Figure 4.** Displacement at the upper left corner of the elastic plate, where the results of SPH and FE-SPH come from references [52] and [50], respectively.

### *3.2. Damaged Cabin cross-Section Models*

When a cabin is damaged and flooding with high momentum flows into it, it will result in an impact load on the cabin's bulkhead. In general, changing the bending stiffness of the cabin's watertight bulkhead can alter load distribution and the likelihood of excessive loads. The effects of stiff and flexible bulkheads with various Young's modulus on the hydrodynamic distribution in the damaged cabin are compared in this section.

The damaged cabin cross-section, shown in Figure 5, weighs 242.349 kg, is 0.7 m wide, and 0.52 m high. The hole is 0.16 m long. We conducted four sets of numerical simulations, which are listed in Table 1, to investigate how different watertight bulkheads affected the distribution of impact loads.

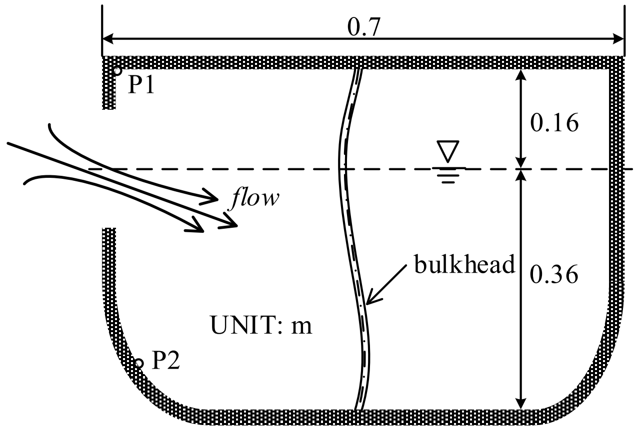


**Figure 5.** Details and dimensions of damaged cabin cross-section models.

**Table 1.** Parameters of the watertight bulkhead used in the numerical simulations.

| Name | Density $\rho$ (kg/m$^3$) | Young's modulus $E$ (Gpa) | Thickness (mm) | $w_1$ (rad/s) | $w_2$ (rad/s) | $w_3$ (rad/s) |
|---|---|---|---|---|---|---|
| Model I | 2500 | 1.8 | 0.04 | 508.4265 | 1401.4972 | 2747.4948 |
| Model II | 2500 | 3.6 | 0.04 | 508.4265 | 1401.4972 | 2747.4948 |
| Model III | 2500 | 7.2 | 0.04 | 508.4265 | 1401.4972 | 2747.4948 |
| Model IV | 2500 | $+\infty$ | 0.04 | 508.4265 | 1401.4972 | 2747.4948 |

### *3.3. Effects of Watertight Bulkheads with Various Young's Modulus*

Figure 6 shows the time histories of the deflections at the middle point of the watertight bulkhead for the three flexible models. It can be seen that the stiffer the watertight bulkhead, the less the deflection, and the maximum deflection of Model I (E = 1.8 Gpa) is approximately three times greater than that of Model III (E = 7.2 Gpa).

As illustrated in Figure 7, the quality of flooding into the models increases at first, then decreases slightly. Before the instant of $t$ = 1.1 s, the quality of the water inflow is close, while, after that, the model with the greater watertight bulkhead elasticity has the greater flooding quality. This agrees with the time histories of deflection shown in Figure 3, especially after the instant of $t$ = 1.1 s, indicating that the elasticity of the watertight bulkhead has an impact on the water inflow, and the influence grows larger as the inflow increases. It should be noted that the fluctuation of quality of Model IV at the final stage in Figure 7 is caused by the non-physical hole.

It can be clearly seen from Figure 8 that the time-history curves of roll motion for the four models are nearly overlapping. This demonstrates that the four models' motion attitudes are consistent, hence the subsequent pressure study may disregard the impact of rolling motion.

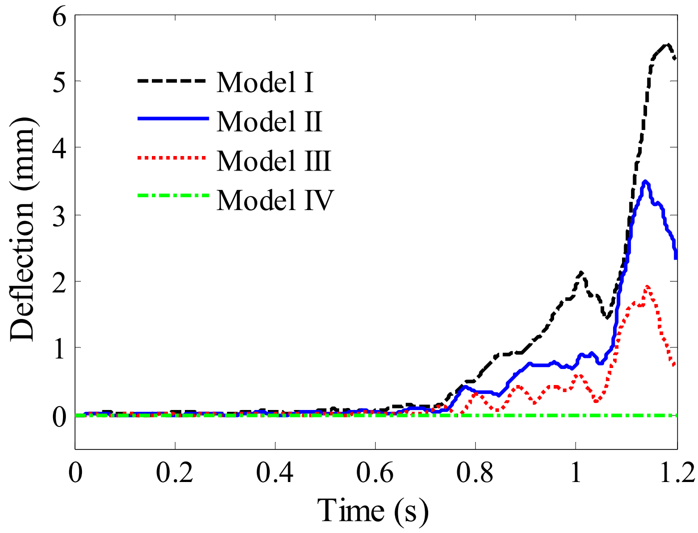


**Figure 6.** Time histories of the deflections at the middle of the bulkheads for Model I~IV.

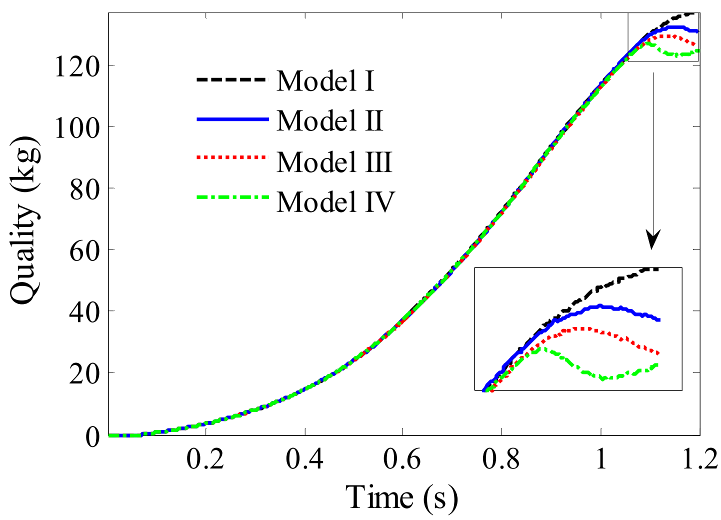


**Figure 7.** Time histories of the amount of flooding for Model I~IV.

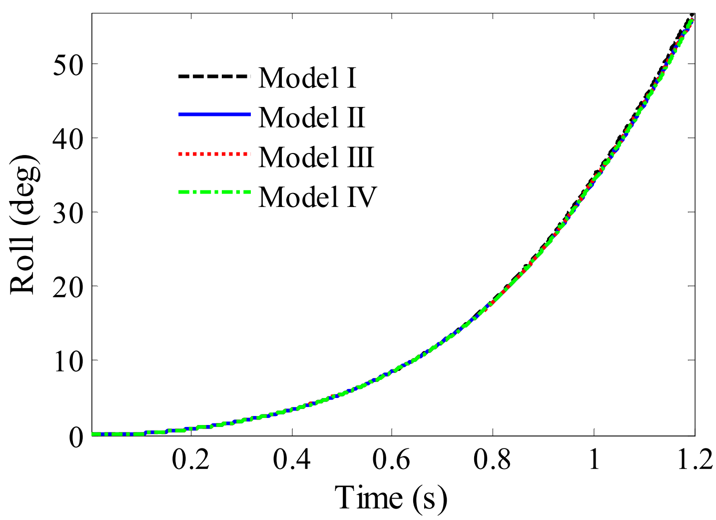


**Figure 8.** Time histories of roll for Model I~IV.

Figure 9 depicts the distributions of the average pressure (0~1.2 s) acting on the watertight bulkheads of various models. The difference in average pressure acting between watertight bulkheads of different stiffnesses is negligible; for individual watertight bulkheads, the closer to the bottom of the cabin, the greater the average pressure, a characteristic resembling the distribution of hydrostatic pressure.

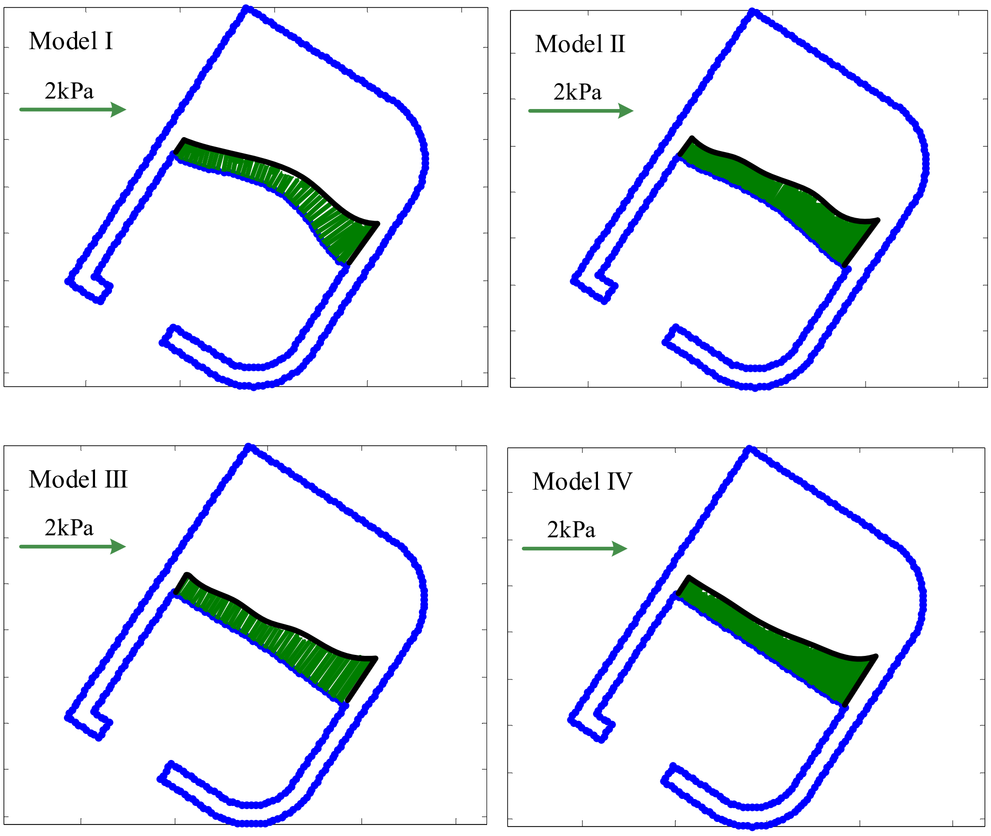


**Figure 9.** Distributions of the average pressure (0~1.2 s) acting on the bulkheads.

Figure 10 shows the distributions of the peak pressure (0~1.2 s) acting on the bulkheads of different models. It is clear that the peak pressure distribution is significantly influenced by stiffness. The watertight bulkhead's peak pressure rises with increasing stiffness, with the peak pressure of Model IV reaching nearly three times that of Model I. Additionally, unlike the distribution of the average pressure (shown in Figure 9), the peak pressure on the two edges of the watertight bulkheads is higher than that at their middle, which needs to be taken into account in the design of the cabin.

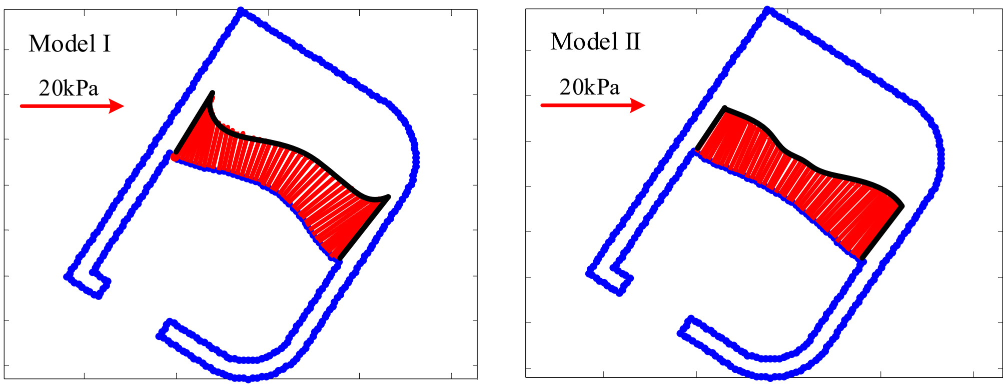


(**a**) (**b**)

**Figure 10.** *Cont.*

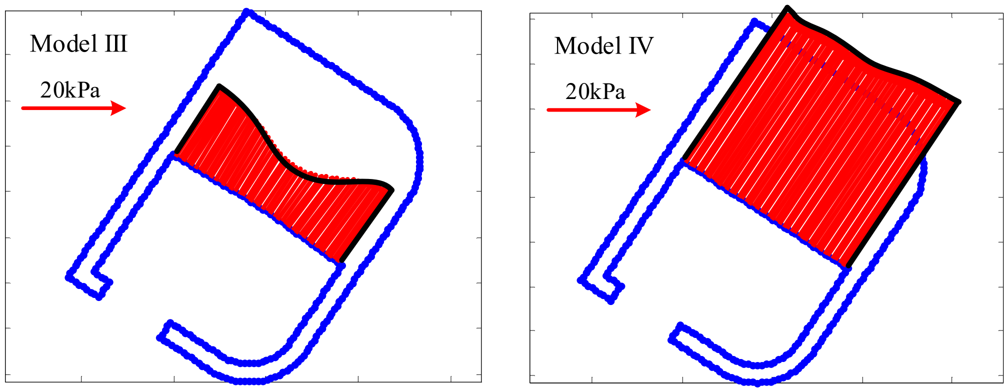


(c) (d)

**Figure 10.** Distributions of the peak pressure (0~1.2 s) acting on the bulkheads.

By influencing the deformation of the watertight bulkheads and the distribution of the load on it, the stiffness of the watertight bulkhead eventually leads to the difference in hydrodynamic distribution throughout the damaged cabin. Figure 11 shows the pressure distribution for various models at $t$ = 1.2 s, and the clear difference in the flow field is visible.

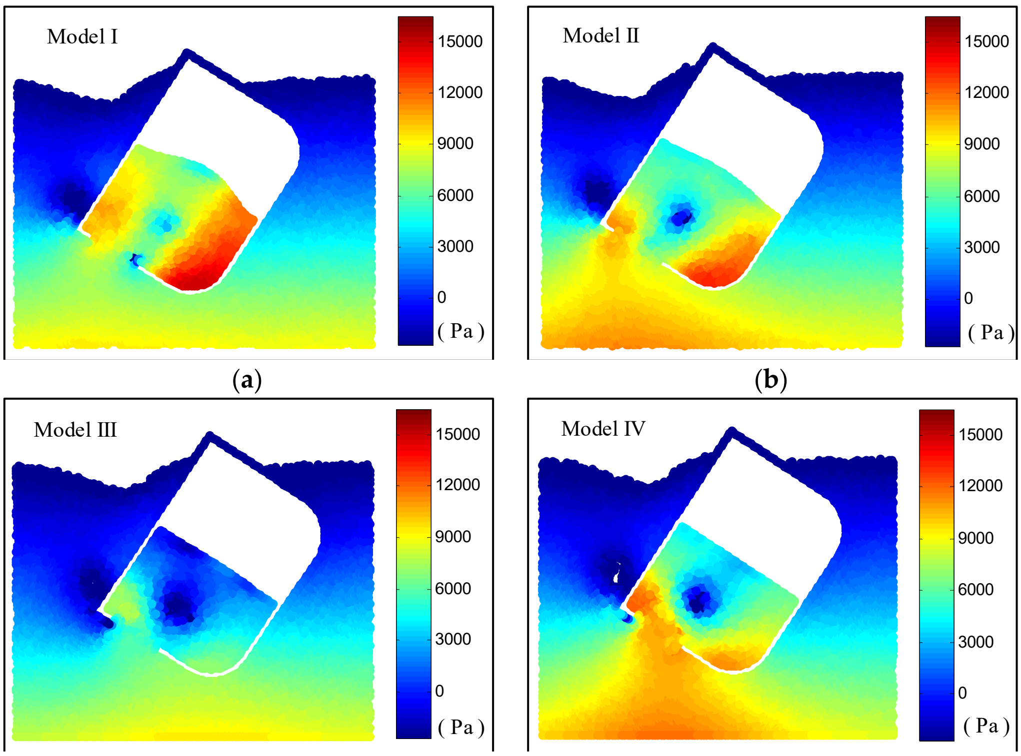


(a) (b) (c) (d)

**Figure 11.** Selected screenshots representing pressure contours of the flooding processes at $t$ = 1.2 s, where (**a**–**d**) corresponds to Model I~IV shown in Table 1, respectively.

Figure 12 displays the time histories of the pressure at monitoring points P1 and P2 for models with rigid and flexible bulkheads. It can be seen that the peak pressures at points P1 and P2 increase as the bulkhead's stiffness increases. Model IV, with a rigid bulkhead, has the highest peak pressure, while Model I, with the bulkhead of the smallest Young's modulus, has a lesser peak pressure.

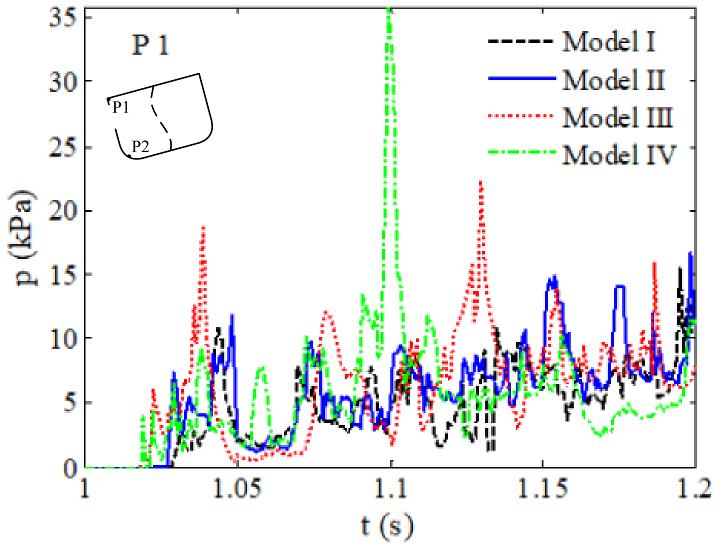


(**a**) Point P1

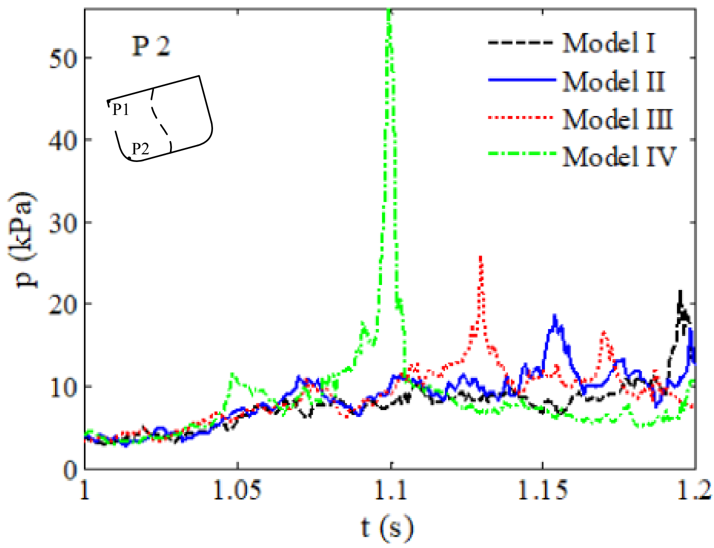


(**b**) Point P2

**Figure 12.** The pressure time histories of monitoring points P1 and P2 on four models.

As listed in Table 2, as compared with Model IV, the peak pressures at points P1 and P2 of Model I are reduced by roughly 57.1% and 61.8%, respectively. In addition, for average pressure, the loads on the two points in Model I are lowered by roughly 34.6% and 20.1%, respectively. According to the comparison, flexible watertight bulkheads often perform better in terms of reducing the peak and average value. This is because the elastic bulkhead can more effectively absorb the energy of flooding and reduce the impact on the other interior bulkhead.

**Table 2.** Peak and average pressures at points P1 and P2.

| Name | Model I | Model II | Model III | Model IV |
|---|---|---|---|---|
| Peak pressure for P1 (kPa) | 15.41 | 16.71 | 22.36 | 35.91 |
| Average pressure for P1 (kPa) | 4.50 | 5.59 | 5.90 | 7.94 |
| Peak pressure for P2 (kPa) | 21.47 | 18.55 | 25.94 | 56.15 |
| Average pressure for P2 (kPa) | 7.59 | 8.70 | 8.88 | 9.50 |

## 4. Conclusions

In this study, the pressure distribution is investigated numerically by the fluid–solid solver coupled with the modified MPS method and the modal superposition model. First, the dam-break wave impact on an elastic plate is performed and the results are in good agreement with the corresponding experimental data, demonstrating the viability of using the solver to simulate such issues. Then, four damaged cabin models with various stiffness watertight bulkheads are numerically simulated and the results are analyzed; the following conclusions are drawn:

- The peak pressure distribution on the flexible bulkhead is larger near both ends and smaller in the center.
- As the bulkhead's flexibility is increased over a range, the peak pressure on the watertight bulkhead is significantly reduced.
- The flexibility of the watertight bulkhead indirectly affects the hydrodynamic pressure distribution of the entire flow field, reducing peak pressure at points on other rigid bulkheads in the cabin (e.g., monitoring points P1 and P2).

The aforementioned findings discover that watertight bulkheads with the appropriate stiffness and material properties can lessen the effect of flooding on the inner wall of a damaged cabin.

**Author Contributions:** Formal analysis, J.W.; funding acquisition, G.Z.; methodology, J.W., G.Z., Y.J. and X.Y.; writing—original draft, J.W.; writing—review and editing, G.Z., Y.J. and X.Y. All authors have read and agreed to the published version of the manuscript.

**Funding:** This research was funded by [National Natural Science Foundation of China] grant number [52061135107], [Fundamental Research Fund for the Central Universities] grant number [DUT20TD108], [Liao Ning Revitalization Talents Program] grant number [XLYC1908027] and [Dalian Innovation Research Team in Key Areas] grant number [No. 2020RT03].

**Institutional Review Board Statement:** Not applicable.

**Informed Consent Statement:** Not applicable.

**Data Availability Statement:** Readers can access our data by sending an email to the authors.

**Acknowledgements:** We thank the computation support of the Supercomputing Center of Dalian University of Technology.

**Conflicts of Interest:** The authors declare no conflict of interest.

## Appendix A

Derivation of the Governing Equations for Cabin's Motion

According to the extended Hamilton's principle [48], the motion of the whole cabin system could be described by Lagrange's Equation, as provided in Equation (A1):

$$\frac{d}{dt}\left(\frac{\partial T}{\partial \dot{\mathbf{X}}}\right) + \frac{\partial V}{\partial \mathbf{X}} - \frac{\partial T}{\partial \mathbf{X}} = \mathbf{Q} \tag{A1}$$

The kinetic and potential energies for the rigid body and flexible beams are given in Equations (A2)–(A5):

$$T_R = \frac{1}{2}\int_R \dot{\mathbf{X}}_R^T \rho \dot{\mathbf{X}}_R dxdy \tag{A2}$$

$$T_F = \frac{1}{2}\int_F \dot{\mathbf{X}}_F^T \rho \dot{\mathbf{X}}_F ds \tag{A3}$$

$$V_R = M_R g Y_R \tag{A4}$$

$$
\begin{aligned}
V_F &= \frac{1}{2}\int_F \frac{d^2\eta}{ds^2} EJ \frac{d^2\eta}{ds^2} ds + M_F g Y_F \\
&= \frac{1}{2}\mathbf{q}^T \mathbf{\Lambda} \mathbf{q} + M_F g \left( Y_R + \sin\theta x_{of} + \cos\theta y_{of} \right)
\end{aligned}
\tag{A5}
$$

where $T_R$, $V_R$, $T_f$, and $V_f$ are the kinetic energies and potential energies for the rigid structure and flexible beam. The kinetic and potential energies for the whole structure could be calculated as Equations (A6) and (A7):

$$
T = T_R + T_F \tag{A6}
$$

$$
V = V_R + V_F \tag{A7}
$$

After substituting Equations (A2)–(A7) into Equation (A1), the governing equations for the dynamics of the damaged cabin structure with rigid/flexible bulkhead are derived in Equations (A8)–(A10):

$$
\begin{aligned}
&\int_f \left( \ddot{\mathbf{X}}_R - \mathbf{R}_R \dot{\theta}^2 \boldsymbol{o}_{R-F} + \mathbf{R}_R \mathbf{U} \ddot{\theta} \boldsymbol{o}_{R-F} - \mathbf{R}_f \dot{\theta}^2 \boldsymbol{\xi} + \mathbf{R}_f \mathbf{U} \ddot{\theta} \boldsymbol{\xi} + 2\mathbf{R}_f \mathbf{U} \dot{\theta} \dot{\boldsymbol{\xi}} + \mathbf{R}_f \ddot{\boldsymbol{\xi}} \right) \rho_l ds \\
&\quad + M_R \ddot{\mathbf{X}}_R + \left( M_R + M_f \right) g \begin{bmatrix} 0 \\ 1 \end{bmatrix} = \mathbf{Q}_X
\end{aligned}
\tag{A8}
$$

$$
\begin{aligned}
&\int_f \begin{pmatrix} \ddot{\mathbf{X}}_R^T + \ddot{\theta} \boldsymbol{o}_{R-F}^T \mathbf{U}^T \mathbf{R}_R^T - \dot{\theta}^2 \boldsymbol{o}_{R-F}^T \mathbf{R}_R^T + \ddot{\theta} \boldsymbol{\xi}^T \mathbf{U}^T \mathbf{R}_f^T \\ + 2\dot{\theta} \dot{\boldsymbol{\xi}}^T \mathbf{U}^T \mathbf{R}_f^T - \dot{\theta}^2 \boldsymbol{\xi}^T \mathbf{R}_f^T + \ddot{\boldsymbol{\xi}}^T \mathbf{R}_f^T \end{pmatrix} \left( \mathbf{R}_R \mathbf{U} \boldsymbol{o}_{R-F} + \mathbf{R}_f \mathbf{U} \boldsymbol{\xi} \right) \rho_l ds \\
&\quad + I_R \ddot{\theta} + M_f \left( \cos\theta x_{of1} + \sin\theta x_{of2} \right) = Q_\theta
\end{aligned}
\tag{A9}
$$

$$
\begin{aligned}
&\int_f \begin{pmatrix} \ddot{\mathbf{X}}_R^T + \ddot{\theta} \boldsymbol{o}_{R-F}^T \mathbf{U}^T \mathbf{R}_R^T - \dot{\theta}^2 \boldsymbol{o}_{R-F}^T \mathbf{R}_R^T + \ddot{\theta} \boldsymbol{\xi}^T \mathbf{U}^T \mathbf{R}_f^T \\ + 2\dot{\theta} \dot{\boldsymbol{\xi}}^T \mathbf{U}^T \mathbf{R}_f^T - \dot{\theta}^2 \boldsymbol{\xi}^T \mathbf{R}_f^T + \ddot{\boldsymbol{\xi}}^T \mathbf{R}_f^T \end{pmatrix} \left( \mathbf{R}_f \begin{bmatrix} 0 \\ 1 \end{bmatrix} \mathbf{\Phi} \right) \rho_l ds \\
&\quad + \mathbf{\Lambda} \mathbf{q} = \mathbf{Q}_q
\end{aligned}
\tag{A10}
$$

where $\mathbf{U}$, $\mathbf{R}_R$, and $\mathbf{R}_F$ are defined in Equations (A11)–(A13):

$$
\mathbf{U} = \begin{bmatrix} 0 & -1 \\ 1 & 0 \end{bmatrix} \tag{A11}
$$

$$
\mathbf{R}_R = \begin{bmatrix} 0 & -1 \\ 1 & 0 \end{bmatrix} \tag{A12}
$$

$$
\mathbf{R}_F = \mathbf{R}_R \mathbf{U} \tag{A13}
$$

In this work, the whole damaged cabin structure is subject to the distributed pressure $P$ only and they are provided in Equations (A14)–(A16):

$$
\mathbf{Q}_X = [Q_1,\ Q_2] = \int_{all} p\mathbf{n} dl \tag{A14}
$$

$$
Q_\theta = Q_3 = \int_{all} p\left( X_p n_y - Y_p n_x \right) dl \tag{A15}
$$

$$
\mathbf{Q}_q = [Q_4,\ Q_5,\ Q_6] = \int_f [(p\mathbf{n}) \cdot \mathbf{e}_w] \mathbf{\Phi} dl \tag{A16}
$$

where $\mathbf{n} = [n_x, n_y]$ is the normal vector of the structure surface pointing towards the inside of the solid boundary and $\mathbf{e}_w$ is the unit vector of $o_{F-w}$ axis.

## References


1. Bhattacharya, B.; Basu, R.; Srinivasan, S. A probabilistic model of flooding loads on transverse watertight bulkheads in the event of hull damage. *J. Ship Res.* **2005**, *49*, 12–23. [CrossRef]
2. Guo, K.; Sun, P.N.; Cao, X.Y.; Huang, X. A 3-D SPH model for simulating water flooding of a damaged floating structure. *J. Hydrodyn.* **2017**, *29*, 831–844. [CrossRef]
3. Ruponen, P. On the effects of non-watertight doors on progressive flooding in a damaged passenger ship. *Ocean. Eng.* **2017**, *130*, 115–125. [CrossRef]
4. Pamuk, M.T. Transient Analysis of Ship Flooding. *Nav. Eng. J.* **2019**, *131*, 121–130.
5. Zhang, G.; Wu, J.; Sun, Z.; el Moctar, O.; Zong, Z. Numerically simulated flooding of a freely-floating two-dimensional damaged ship section using an improved MPS method. *Appl. Ocean. Res.* **2020**, *101*, 102207.
6. Hwang, S.C.; Park, J.C.; Gotoh, H.; Khayyer, A.; Kang, K.J. Numerical simulations of sloshing flows with elastic baffles by using a particle-based fluid–structure interaction analysis method. *Ocean. Eng.* **2016**, *118*, 227–241. [CrossRef]
7. Chen, X.; Zhang, Y.; Wan, D. Numerical Study of 3-D Liquid Sloshing in an Elastic Tank by MPS-FEM Coupled Method. *J. Ship Res.* **2019**, *63*, 143–153. [CrossRef]
8. Sun, X.; Zhong, Y.; Bian, F.; Liu, C.; Yin, Y. Numerical Computation of Sloshing-Induced Force in Complex Ship Tanks under the Excitation of Ship Rolling Motion Based on the MPS Method. *Appl. Sci.* **2022**, *12*, 5130. [CrossRef]
9. Wang, Q.Y.; Lin, G.M.; Jiang, L.; Zheng, G.F.; Chen, J.J. Numerical and experimental study of anti-slosh performance of combined baffles in partially filled tank vehicles. *Int. J. Press. Vessel. Pip.* **2022**, *196*, 104555. [CrossRef]
10. Zhang, C.; Sun, X.; Wang, P.; Chen, L.; Ning, D. Hydrodynamics of a floating liquid-tank barge adjacent to fixed structure in beam waves. *Phys. Fluids* **2022**, *34*, 047114. [CrossRef]
11. Huang, X.; Hu, H.; Zhang, A.M.; Chen, G.Q. Simulation of the early stage water flooding through an opening using boundary element method. *Ocean. Eng.* **2019**, *186*, 106086. [CrossRef]
12. Bennett, S.S.; Phillips, A.B. Experimental investigation of the influence of floodwater due to ship grounding on motions and global loads. *Ocean. Eng.* **2017**, *130*, 49–63. [CrossRef]
13. Rodrigues, J.M.; Soares, C.G. Still water vertical loads during transient flooding of a tanker in full load condition with a probabilistic damage distribution. *Ocean. Eng.* **2017**, *129*, 480–494. [CrossRef]
14. Yu, B.; Zhang, W.; Chen, J.; Yu, X.; Yu, Y.; Zhou, J. Time-domain simulation of inlet of damaged cabin of fishing boats and research on damaged cabin stability and pressure distribution based on CFD. *J. Dalian Univ. Technol.* **2021**, *61*, 355–367.
15. Cao, X.Y.; Tao, L.; Zhang, A.M.; Ming, F.R. Smoothed particle hydrodynamics (SPH) model for coupled analysis of a damaged ship with internal sloshing in beam seas. *Phys. Fluids* **2019**, *31*, 032103. [CrossRef]
16. Gu, Y.; Day, A.; Boulougouris, E.; Dai, S. Experimental investigation on stability of intact and damaged combatant ship in a beam sea. *Ships Offshore Struct.* **2018**, *13*, 322–338. [CrossRef]
17. Siddiqui, M.A.; Greco, M.; Lugni, C.; Faltinsen, O.M. Experimental studies of a damaged ship section in forced heave motion. *Appl. Ocean. Res.* **2019**, *88*, 254–274. [CrossRef]
18. Hirt, C.W.; Nichols, B.D. Volume of fluid (VOF) method for the dynamics of free boundaries. *J. Comput. Phys.* **1981**, *39*, 201–225. [CrossRef]
19. Unverdi, S.O.; Grétar, T. A front-tracking method for viscous, incompressible, multi-fluid flows. *J. Comput. Phys.* **1992**, *100*, 25–37. [CrossRef]
20. Sussman, M.; Smereka, P.; Osher, S. A Level Set Approach for Computing Solutions to Incompressible Two-Phase Flow. *J. Comput. Phys.* **1994**, *114*, 146–159. [CrossRef]
21. Peng, D.; Merriman, B.; Osher, S.; Zhao, H.; Kang, M. A PDE-based fast local level set method. *J. Comput. Phys.* **1999**, *155*, 410–438. [CrossRef]
22. Veldman, A.E.; Gerrits, J.; Luppes, R.; Helder, J.A.; Vreeburg, J. The numerical simulation of liquid sloshing on board spacecraft. *J. Comput. Phys.* **2007**, *224*, 82–99. [CrossRef]
23. Koshizuka, S.; Oka, Y. Moving-Particle Semi-Implicit Method for Fragmentation of Incompressible Fluid. *Nucl. Sci. Eng.* **1996**, *123*, 421–434. [CrossRef]
24. Koshizuka, S.; Nobe, A.; Oka, Y. Numerical analysis of breaking waves using the moving particle semi-implicit method. *Int. J. Numer. Methods Fluids* **1998**, *26*, 751–769. [CrossRef]
25. Liu, G.; Liu, M. *Smoothed Particle Hydrodynamics: A Meshfree Particle Method*; World Scientific Publishing: Singapore, 2003.
26. Gingold, R.A.; Monaghan, J.J. Smoothed Particle Hydrodynamics—Theory and Application To Non-Spherical Stars. *Mon. Not. R. Astron. Soc.* **1977**, *181*, 375–389. [CrossRef]
27. Lucy, L.B. A numerical approach to the testing of the fission hypothesis. *Astron. J.* **1977**, *82*, 1013–1024. [CrossRef]
28. Sun, Z.; Jiang, Y.C.; Zhang, G.Y.; Zong, Z.; Xing, J.T.; Djidjeli, K. Slamming load on trimaran cross section with rigid and flexible arches. *Mar. Struct.* **2019**, *66*, 227–241. [CrossRef]
29. Zha, R.S.; Peng, H.; Qiu, W. Solving 2-D Slamming Problems by an Improved Higher-Order Moving Particle Semi-Implicit Method. *J. Ship Res.* **2021**, *65*, 194–222. [CrossRef]

30. Hwang, S.C.; Khayyer, A.; Gotoh, H.; Park, J.C. Development of a fully Lagrangian MPS-based coupled method for simulation of fluid–structure interaction problems. *J. Fluids Struct.* **2014**, *50*, 497–511. [CrossRef]
31. Antoci, C.; Gallati, M.; Sibilla, S. Numerical simulation of fluid-structure interaction by SPH. *Comput. Struct.* **2007**, *85*, 879–890. [CrossRef]
32. Mitsume, N.; Yoshimura, S.; Murotani, K.; Yamada, T. Mps-Fem Partitioned Coupling Approach for Fluid-Structure Interaction with Free Surface Flow. *Int. J. Comput. Methods* **2014**, *11*, 1350101. [CrossRef]
33. Mitsume, N.; Yoshimura, S.; Murotani, K.; Yamada, T. Improved MPS-FE Fluid-Structure Interaction Coupled Method with MPS Polygon Wall Boundary Model. *Comput. Model. Eng. Sci.* **2014**, *101*, 229–247.
34. Khayyer, A.; Gotoh, H. Modified Moving Particle Semi-implicit methods for the prediction of 2D wave impact pressure. *Coast. Eng.* **2009**, *56*, 419–440. [CrossRef]
35. Chen, X.; Xi, G.; Sun, Z.-G. Improving stability of MPS method by a computational scheme based on conceptual particles. *Comput. Methods Appl. Mech. Eng.* **2014**, *278*, 254–271. [CrossRef]
36. Khayyer, A.; Gotoh, H. Enhancement of stability and accuracy of the moving particle semi-implicit method. *J. Comput. Phys.* **2011**, *230*, 3093–3118. [CrossRef]
37. Daneshvar, F.A.; Rakhshandehroo, G.R.; Talebbeydokhti, N. New modified gradient models for MPS method applied to free-surface flow simulations. *Appl. Ocean. Res.* **2017**, *66*, 95–116. [CrossRef]
38. Khayyer, A.; Gotoh, H. Development of CMPS Method for Accurate Water-Surface Tracking in Breaking Waves. *Coast. Eng. J.* **2018**, *50*, 179–207. [CrossRef]
39. Xiao, H.; Jin, Y.-C. Development of explicit moving particle simulation method with applications. *Comput. Fluids* **2022**, *235*, 105270. [CrossRef]
40. Chen, X.; Sun, Z.G.; Liu, L.; Xi, G. Improved MPS method with variable-size particles. *Int. J. Numer. Methods Fluids* **2016**, *80*, 358–374. [CrossRef]
41. Tang, Z.Y.; Zhang, Y.L.; Wan, D.C. Multi-Resolution MPS Method for Free Surface Flows. *Int. J. Comput. Methods* **2016**, *13*, 1641018. [CrossRef]
42. Tanaka, M.; Cardoso, R.; Bahai, H. Multi-resolution MPS method. *J. Comput. Phys.* **2018**, *359*, 106–136. [CrossRef]
43. Nabian, M.A.; Farhadi, L. MR-WC-MPS: A Multi-Resolution WC-MPS Method for Simulation of Free-Surface Flows. *Water* **2019**, *11*, 1349. [CrossRef]
44. Liu, X.X.; Zhang, S. Development of adaptive multi-resolution MPS method for multiphase flow simulation. *Comput. Methods Appl. Mech. Eng.* **2021**, *387*, 114184. [CrossRef]
45. Shakibaeinia, A.; Jin, Y.-C. A weakly compressible MPS method for modeling of open-boundary free-surface flow. *Int. J. Numer. Methods Fluids* **2010**, *63*, 1208–1232. [CrossRef]
46. Sun, Z.; Djidjeli, K.; Xing, J.T.; Cheng, F. Coupled MPS-modal superposition method for 2D nonlinear fluid-structure interaction problems with free surface. *J. Fluids Struct.* **2016**, *61*, 295–323. [CrossRef]
47. Sun, Z.; Djidjeli, K.; Xing, J.T. Modified MPS method for the 2D fluid structure interaction problem with free surface. *Comput. Fluids* **2015**, *122*, 47–65. [CrossRef]
48. Benaroya, H.; Wei, T.; Kuchnicki, S.; Dong, P. Extended Hamilton'S Principle for Fluid-Structure Interaction. *Proc. Inst. Mech. Eng. Part K J. Multi Body Dyn.* **2003**, *217*, 153–170.
49. Newmark, N.M. A method of computation for structural dynamics. *J. Eng. Mech. Div.* **1959**, *85*, 67–94. [CrossRef]
50. Hu, D.; Long, T.; Xiao, Y.; Han, X.; Gu, Y. Fluid–structure interaction analysis by coupled FE–SPH model based on a novel searching algorithm. *Comput. Methods Appl. Mech. Eng.* **2014**, *276*, 266–286. [CrossRef]
51. Koshizuka, S.; Oka, Y.; Tamako, H. *A Particle Method for Calculating Splashing of Incompressible Viscous Fluid*; American Nuclear Society, Inc.: La Grange Park, IL, USA, 1995.
52. Rafiee, A.; Thiagarajan, K.P. An SPH projection method for simulating fluid-hypoelastic structure interaction. *Comput. Methods Appl. Mech. Eng.* **2009**, *198*, 2785–2795. [CrossRef]
53. Wu, J.; Sun, Z.; Jiang, Y.; Zhang, G.; Sun, T. Experimental and numerical study of slamming problem for a trimaran hull. *Ships Offshore Struct.* **2021**, *16*, 46–53. [CrossRef]